Application of a Substructure-Based Hardening Model to Copper under Loading Path Changes

S. MAHESH, C.N. TOMÉ, R.J. McCABE, G.C. KASCHNER, I.J. BEYERLEIN, and A. MISRA

In addition to texture, plastic anisotropy of a polycrystalline fcc metal stems from the directional nature of the dislocation substructure within individual grains. This produces the marked work hardening or softening observed immediately following load path changes. Following the framework of Peeters *et al.*,[1,2] in bcc steel, we develop a dislocation substructure evolution-based stage III hardening model for copper, capable of capturing the constitutive response under load path changes. The present model accounts for the more complicated substructure geometry in fcc metals than in bcc. Using an optimization algorithm, the parameters governing substructure evolution in the model are fit to experimental stress-strain curves obtained during compression along the three orthogonal directions in samples previously rolled to various reductions. These experiments approximate monotonic, reverse, and cross-load paths. With parameters suitably chosen, the substructure model, embedded into a self-consistent polycrystal plasticity model, is able to reproduce the measured flow stress response of copper during load path change experiments. The sensitivity of the parameters to the assumed substructure geometry and their uniqueness are also discussed.

I. INTRODUCTION

THE explosive growth of understanding over the last decade or so, of plastic deformation processes in polycrystals at different length scales (especially at the substructure level), obtained largely through electron microscopy, has brought us near the point where such information may be incorporated in models of bulk polycrystal response. Such substructure-based hardening models could supplement or supplant traditional grain hardening models that resort to phenomenological considerations at the length scale of the grain. While on the one hand a substructure-based approach is much more detailed and intensive than the traditional hardening laws, on the other hand, due to the much more detailed description of the internal *state* of a grain used by the substructure-based approach, it can capture, for instance, transient response during nonmonotonic loading, which lies beyond the capabilities of typical grain-level phenomenological approaches.

Most polycrystal models available in the literature concerned with reproducing the texture evolution and the anisotropy of the aggregate are usually based on relatively simple hardening laws for the active slip systems (Balasubramanian and Anand,[3] Tomé *et al.*,[4,5] Kok *et al.*,[6] and Kocks *et al.*[7]). For example, Tomé *et al.*[4] consider an extended Voce law of slip system hardening to describe the effect of texture evolution upon the *monotonic* stress-strain response of oxygen free high conductivity (OFHC) copper:

$$\tau_s^c(\Gamma) = \tau_0 + (\tau_1 + \theta_1\Gamma)\,[1 - \exp\,(-\theta_0\,\Gamma/\tau_1)] \quad [1]$$

Here, the evolution of τ_s^c, the critical resolved shear stress in slip system s, is given as a function of the accumulated strain in the grain Γ. The parameter τ_0 is the initial yield stress, $\tau_0 + \tau_1$ the back-extrapolated yield stress, and θ_0 and θ_1 the initial and final hardening rates, respectively. Such an expression accounts for dislocation hardening in a qualitative way and succeeds in accounting for texture effects on the overall stress-strain response[4] associated with monotonic loading. However, Tomé *et al.*[4] could not find a unique set of hardening parameters that accounts for the polycrystal mechanical behavior under different loadings: tension, compression, and torsion. They concluded that crystal orientation effects account for about half of the observed von Mises yield stress discrepancy between large strain tension, compression, and torsion and attributed the other half to differences in the dislocation structure associated with each deformation mode. Another disadvantage of simple hardening rules such as Eq. [1] is that they do not suffice to predict the transients associated with strain path changes. To capture the observed transients, one needs a kinematic hardening law, which accounts for the directionality and evolution of dislocation structures inside the grains.

More recently, models have been proposed that focus on predicting dislocation density evolution, and connecting it with the macroscopic yield stress (*e.g.*, Kocks and Mecking,[8] Teodosiu and Hu,[9] Hahner,[10] and Pantleon[11]). These substructure-based models, improve upon laws like Eq. [1], but disregard the dependence of the dislocation structure and density on grain orientation. This deficiency is overcome in the work of Estrin *et al.*[12] and Tóth *et al.*[13] for copper, and Baik *et al.*[14] for aluminum, which incorporate dislocation density evolution in their hardening laws and run polycrystal simulations of *monotonic loading*. The work of Peeters *et al.*[1] for steel is a first attempt at predicting transients associated with *strain path changes* using the preceding approach. In parallel with this modeling effort, there has lately been an increased interest in characterizing experimentally the mechanical response and microstructure evolution associated with strain path changes (Gracio *et al.*,[15] Rauch *et al.*,[16] Barlat *et al.*,[17] and Lopes *et al.*[18]). Table I provides a further summary of some of the approaches described previously.

In this work, we develop a substructure evolution model of OFHC copper grains that generates a hardening law fed into

S. MAHESH, Postdoctoral, C.N. TOMÉ, R.J. McCABE, G.C. KASCHNER, and A. MISRA, Technical Staff Members, Materials Science and Technology Division, and I.J. BEYERLEIN, Theoretical Division, are with Los Alamos National Laboratory, Los Alamos, NM 87545. Contact e-mail: tome@lanl.gov

Manuscript submitted December 5, 2003.

Table I. Summary of Some of the Hardening Models Available in the Literature; only fitting parameters used in the hardening law of each model have been counted toward the entry in column 4

Reference	Material	Modeling Goals	Parameters	Hardening Model
Balasubramanian and Anand[3]	Ti	mechanical behavior and texture in monotonic tests	9	Voce-like
Tomé *et al.*[4]	Cu	mechanical behavior in monotonic tests	4	Voce-like
Kok *et al.*[6]	steel	mechanical behavior in monotonic tests in stage IV with temperature and strain-rate dependence	17	MTS-like
Tóth *et al.*[13]	Cu	mechanical behavior in monotonic tests in stages IV and V	12	substructure evolution
Baik *et al.*[14]	Al	cell size and equivalent stress evolution in reverse tests	12	substructure evolution
Peeters *et al.*[1]	steel	mechanical response during monotonic, reverse, and cross tests in stage III	12	substructure evolution

a self-consistent polycrystal model. We calibrate and test our model under monotonic and nonmonotonic loading paths (reverse and cross loadings). The reason is that while both texture and microstructure underlie the anisotropic response of polycrystalline materials subjected to most loading paths, during reverse loading, anisotropy is entirely attributable to microstructure alone. The material shows softening, a phenomenon termed the *Bauschinger effect*. On the other hand, the *cross effect*, which manifests as hardening or strain softening during cross loading (Barlat *et al.*[17] and Aernoudt *et al.*[19] (Figure 20) has both texture and microstructure causes.

Dislocation structures within grains are the predominant microstructure contribution to the anisotropy of pure polycrystalline copper. It has been extensively observed (*e.g.*, Malin and Hatherly,[20] Gil Sevillano and Torrealdea,[21] Christoffersen and Leffers,[22] and Huang[23]) that even after only a few percent straining of copper, microstructure develops, which shows relatively dislocation-depleted regions called cell blocks enclosed by geometrically necessary cell block boundaries (CBBs). Dislocations in the CBBs are variously referred to as wall or forest dislocations. In their extensive studies of fcc metal substructures, their evolution, and structural transitions, Hughes, Hansen, and co-workers (Bay *et al.*,[24] Hughes and Nix,[25] and Hughes and Hansen[26,27]) have classified CBBs as dense dislocation walls, microbands, lamellar bands, *etc*. The cell blocks in turn contain cells that are demarcated by incidental dislocation structures called cell boundaries (CBs) or tangles. Anisotropic strain hardening at the grain level results from the presence of cells and cell blocks, which influence slip in each grain and the stress needed for their activation. In turn, slip affects the formation and development of CBs and CBBs by influencing the rates of multiplication, storage, and annihilation of dislocations in them. Grain-level anisotropic response is thus a consequence of complex, tightly coupled processes involving slip activity, and microstructure evolution.

A number of models (*e.g.*, Kocks *et al.*,[30] Kubin and Lépinoux,[31] and Tóth *et al.*[13]) attempt to account for the microstructure of the grain with two state variables, most commonly ρ_{CB}, the density of the mobile dislocations, and ρ_{CBB}, the density of the wall or forest dislocations. Such models succeed in predicting the work hardening with monotonic strain paths but fail in predicting the stress-strain response associated with load path change tests. Kubin[32] has pointed out that these simple models fail because two state variables are inadequate to capture the complex interactions between dipolar and multipolar ensembles, sessile junctions, mobile dislocations on intersecting slip systems, and tangled dislocations. He suggests that substructure models must distinguish between dislocations of the same or opposite sign, of different characters, of different Burgers vectors, and account for their interactions. Another fundamental limitation of models of the substructure as a uniform distribution of dislocations is that they are incapable of coupling the evolving internal stress in the grain to the evolving substructral length scale.

The model of Peeters *et al.*[1,2] goes in the direction of overcoming these limitations. Based on experimental observations of the substructure, this model predetermines a certain number of *potential* CBB orientations, n_{CBB}, relative to the crystal lattice. The state of the grain is then represented by $2n_{CBB} + 1$ dislocation densities. The list of state variables consists of two dislocation densities associated with each of the n_{CBB} CBB planes: *viz.* ρ_i^{wd}, which do not have a polarity; ρ_i^{wp}, which do have a polarity; for $i = 1, \ldots, n_{CBB}$, and, a nonpolar dislocation density ρ corresponding to the overall density of CBs in the grain. Using this expanded set of state variables, Peeters *et al.* are able to go beyond the two state variable models and capture the Bauschinger and cross effects in addition to monotonic hardening behavior of interstitial free (IF) steel with remarkable accuracy. The increased complexity of such a model necessitates the introduction of additional parameters to describe the evolution and interaction of the different dislocation populations.

In the present work, we use the Peeters *et al.* framework to model plastic deformation under path changes of fcc copper. Using the optimization algorithm described in the Appendix, we fit the hardening parameters of the model (Section II–A) so that macroscopic predictions of a viscoplastic polycrystal model (Lebensohn and Tomé[33]) agree with experimentally observed responses under monotonic, reverse, and cross-loading paths. We compare the measured and predicted responses in view of the assumptions of the model in Section III, and analyze these results in light of the model assumptions and our present understanding of substructural mechanisms in Section IV.

II. THE HARDENING MODEL

A. *Dislocation Density Evolution*

In this section, we summarize the model of Peeters *et al.*[1] as applied to the present copper study. The first task in applying the model is to define the orientations of potential CBB planes relative to the lattice. While this is discussed in Section B, let us for now suppose that we have identified n_{active} planes out of $n_{\text{CBB}} = 4$ crystallographic planes available to fcc grains undergoing $\langle 110 \rangle \langle 111 \rangle$ slip, as the "active" slip planes parallel to which CBBs may form. Let $\mathbf{u}_i^w$ denote the unit normal to each set of parallel slip planes, with an arbitrary but consistent sign and similarly, let $\mathbf{u}_s^b$ denote the unit vector along the slip directions again, with an arbitrary but consistent sense. In an fcc crystal deforming plastically by $\langle 110 \rangle \langle 111 \rangle$ slip, $s = 1, \ldots, 12$, and $i = 1, \ldots, 4$. Slip information is conveyed to the dislocation evolution procedure through two key variables: the total slip activity on each slip plane, $\dot{\Gamma}_i = \sum_{\{s\,:\,\mathbf{u}_s^b \cdot \mathbf{u}_i^w = 0\}} |\dot{\gamma}_s|$, and the signed dislocation flux into CBB i, $\Phi_i = \sum_s \dot{\gamma}_s \mathbf{u}_s^b \cdot \mathbf{u}_i^w / \mathrm{b}$. Here, $\dot{\gamma}_s$ is the slip rate on the sth of the 12 slip systems of the fcc grain, and b denotes the magnitude of Burgers vector.

According to the model, nonpolar dislocation densities associated with active and inactive planes evolve differently as follows:

$$\dot{\rho}_i^{wd} = \begin{cases} (I^{wd}\sqrt{\rho_i^{wd}} - R^{wd}\rho_i^{wd})\dot{\Gamma}_i/\mathrm{b} & \text{if plane } i \text{ is active,} \\ -R_{ncg}\rho_i^{wd}\dot{\Gamma}_{\text{new}}/\mathrm{b} & \text{if plane } i \text{ is inactive.} \end{cases} \quad [2]$$

$\dot{\Gamma}_{\text{new}}$ is the total slip rate on the currently active slip planes. Thus, according to Eq. [2], the nonpolar dislocation density of active planes grow while that of inactive planes dwindle. The evolution of the polar dislocation density on CBB i depends upon Φ_i, its dislocation flux, as follows:

$$\dot{\rho}_i^{wp} = \begin{cases} (\text{sign}\,(\Phi_i) I^{wp}\sqrt{\rho_i^{wd} + |\rho_i^{wp}|} - R^{wp}\rho_i^{wd})\,|\Phi_i| \\ \qquad \text{if plane } i \text{ is active, and } \Phi_i \text{ has undergone no sign reversal,} \\ -R_{ncg}\rho_i^{wp}\dot{\Gamma}_{\text{new}}/\mathrm{b} \\ \qquad \text{if plane } i \text{ is inactive, and } \Phi_i \text{ has undergone no sign reversal,} \\ -R_{\text{rev}}\rho_i^{wp}|\Phi_i| \\ \qquad \text{if plane } i \text{ is active, and } \Phi_i \text{ has undergone sign reversal,} \\ 0, \quad \text{otherwise.} \end{cases} \quad [3]$$

Finally, for the evolution of the grain-averaged CB density, Peeters *et al.* assume

$$\dot{\rho} = \left(I\sqrt{\rho} - R\rho - \psi R_2 \rho \frac{\rho_{\text{bausch}}}{2\rho_{\text{sat}}^{wp}} \right) \sum_s |\dot{\gamma}_s|/\mathrm{b}, \quad [4]$$

where $\psi = 1$ or 0 according to whether the dislocation flux into at least one of the active CBB planes has changed sign, ρ_{bausch} denotes the total ρ^{wp} content of the active CBB planes whose dislocation flux is reversed, and ρ_{sat}^{wp} denotes the saturation value of the polarized dislocation density, ρ^{wp}. Unlike ρ^{wd}, the growth or diminution of ρ^{wp} on a CBB depends on the mobile dislocation flux into it and not on slip activity parallel to it. The mechanisms implied by Eqs. [3] and [4] are consistent with the TEM observations of Christodoulou *et al.*[34] during reverse tensile experiments.

We refer to Peeters *et al.*[1] for the physical reasoning underlying these evolution equations. Broadly, the I parameters stand for dislocation multiplication coefficients, while the R parameters refer to dislocation annihilation rates. Peeters *et al.* assume an expression for the inhomogeneous cut-through of pre-existing dislocation walls by the formation of microbands. Figure 1 shows that such cut-through also occurs in fcc copper. However, this phenomenon is poorly understood and its form, as assumed in Peeters *et al.*'s[1] Eq. [8], appears to make the flow stress predictions dependent on the simulation time-step. We therefore do not include it in the present calculations, and expect to capture its effect on average through homogeneous annihilation of inactive CBBs *via* Eq. [2].

The current state of the grain determines the critical resolved shear stress of each of its slip systems as follows:

$$\tau_s^c = \tau^0 + (1-f)\tau^{\text{CB}} + f \sum_{i=1}^{4} \tau_{is}^{\text{CBB}}, \quad [5]$$

where $\tau^{\text{CB}} = \alpha G \mathrm{b}\sqrt{\rho}$, and τ_{is}^{CBB} represents the hardening of slip system s by CBB i. The term f is a parameter denoting

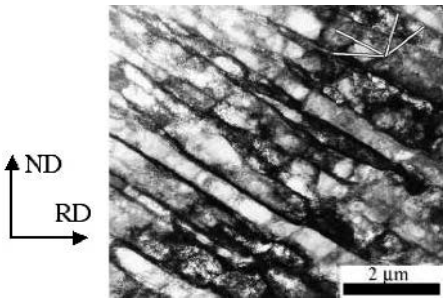

(*a*)

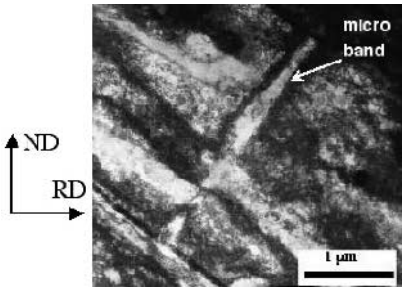

(*b*)

Fig. 1—Transmission electron microscopy (TEM) image of the microstructure of copper (*a*) after rolling to 50 pct reduction and (*b*) immediately after load-crossing by compression along the transverse direction showing the "cut-through" of a CBB formed during the original load path by a microband formed by the slip activity in the cross loading path. Similar dislocation activity during load crossing can also be expected for smaller rolling reductions within the stage III hardening regime.

the volume fraction of CBB in the grain. This latter is known to depend upon the spacing between CBBs i as

$$\tau_{is}^{\mathrm{CBB}} = \frac{\alpha G \mathrm{b}}{d_i} \mathbf{u}_s^b \cdot \mathbf{u}_i^w \qquad [6]$$

Here, $0 < \alpha < 0.5$ represents the dislocation interaction parameter, G the shear modulus of the material, and d_i the average spacing between the ith set of parallel CBBs so that $d_i/\mathbf{u}_s^b \cdot \mathbf{u}_i^w$ is the intercept of slip system s between them. Equation [6] thus represents a directional Hall–Petch type augmentation of the internal stress due to the presence of the CBBs in the grain. The CBB spacing, $d_i/\mathbf{u}_s^b \cdot \mathbf{u}_i^w$ for slip system s are thus taken as the characteristic length scale of importance. $0 \leq f \leq 1$ is the volume fraction of CBBs in the grain, which is assumed fixed in the course of deformation (Argon and Haasen[35] offer justification during stage III). Also, as pointed out by Lopes *et al.*,[18] α may vary from system to system, so as used here, it represents an average over systems. It is known (Godfrey and Hughes[36]) that $d_i = K/\sqrt{\rho_{\mathrm{CBB}}}$, where K is a constant of the order of unity. In the present case, where two wall populations are considered, assuming

$$d_i = \frac{K}{\left[\sqrt{|\rho_i^{wp}|}\,\mathrm{sign}\,(\rho_i^{wp}) + \sqrt{|\rho_i^{wd}|}\right]} \qquad [7]$$

and using Eq. [6] with $\alpha' = \alpha/K$, we obtain

$$\tau_{is}^{\mathrm{CBB}} = \alpha' G \mathrm{b} \left(\sqrt{|\rho_i^{wp}|}\mathbf{u}_s^b \cdot \mathbf{u}_i^w\,\mathrm{sign}\,(\rho_i^{wp}) + \sqrt{\rho_i^{wd}}\,\mathbf{u}_s^b \cdot \mathbf{u}_i^w\right). \qquad [8]$$

The first term involves ρ^{wp}, and together with the decrease in ρ according to Eq. [4], this term is responsible for the Bauschinger effect upon load reversal. Equation [8] is different from the expression of Peeters *et al.* only in that $\alpha = \alpha'$ always in their expression. We will see in Section III that $\alpha \neq \alpha'$ is needed to reproduce the cross-test data in copper.

It should be emphasized that the Peeters *et al.* model is strictly a stage III model (von Mises strain $\lesssim 0.3$ in copper); dislocation populations, ρ_i^{wd}, ρ_i^{wp}, and ρ, eventually saturate with continuing deformation to ρ_∞^{wd}, ρ_∞^{wp}, and ρ_∞, respectively, where

$$\rho_\infty^{wd} = (I^{wd}/R^{wd})^2,$$

$$\rho_\infty^{wp} = \frac{1}{2}\left(\frac{I^{wp}}{R^{wp}}\right)^2\left[1 + \sqrt{1 + 4\left(\frac{I^{wd}R^{wd}}{I^{wp}R^{wd}}\right)^2}\right], \qquad [9]$$

and

$$\rho_\infty = (I/R)^2.$$

Saturation of dislocation densities will result in constancy of the critical resolved shear stresses in Eq. [5] and therefore the constancy of the macroscopic flow stresses. Stage IV hardening behavior shown by fcc metals and characterized by linear hardening to large strains (Cu: Bassim and Liu;[37] and Ni, Co, Al, Ni-Co alloys: Hughes and Nix[25]) cannot be captured by this model.

We embed the preceding model, which supplies a hardening law into the viscoplastic self consistent (VPSC) polycrystal plasticity code (Kocks *et al.*[38] and Lebensohn and Tomé[33]). VPSC assumes a viscoplastic constitutive law for the activity of each slip system s

$$\frac{\dot{\gamma}_s}{\dot{\gamma}_0} = \left(\frac{\boldsymbol{\sigma} : \boldsymbol{m}^s}{\tau_s^c}\right)^n, \quad s = 1, \ldots, 12 \qquad [10]$$

where $\dot{\gamma}_s/\dot{\gamma}_0$ is the scaled shear rate in slip system s, $\sigma : \mathrm{m}^s$ denotes the resolved shear stress on slip system s due to grain stress $\boldsymbol{\sigma}$, and n determines the rate sensitivity. As $n \gg 1$, the grain response becomes rate insensitive.

Unlike the Taylor–Bishop–Hill or the Sachs approach, VPSC does not impose the macroscopic strain rate or stress upon each grain. Instead, grain strain rate is determined self-consistently by embedding the grain in a homogeneous effective medium whose properties are the average properties of other grains. Because of its more realistic nonenforcement of the macroscopic strain rate on each grain, fewer slip systems are activated in the VPSC approach in each grain. This is of much significance to the present hardening model since slip activity affects the evolution rates of the various families of dislocations through $\dot{\Gamma}_i$ and Φ_i.

The evolution equations Eqs. [2] through [5] involve $n_{\mathrm{param}} = 13$ unknowns (I, I^{wp}, I^{wd}, R, R^{wp}, R^{wd}, R_{ncg}, R_{rev}, R_2, α, α', f, τ^0). Ideally, the dynamics of dislocation interaction between the various families of dislocations would be known, for example, from dislocation dynamics calculations. Such information will provide values or plausible ranges for the fitting parameters. Unfortunately, to our knowledge, this information does not presently exist, but can be expected in the near future. Presently, therefore, we will attempt to *fit* these parameters in order to reproduce the stress-strain curves of various monotonic and path change experiments. For such a complex spectrum of parameters, the usual approach of manually guessing, testing, and modifying the parameters is likely to be unsuccessful. For this reason, we adopt a numerical procedure that uses the optimization methods to find parameters, as described in Appendix A. The nature and consequences of the present approach will be further discussed in Sections IV and V.

B. *Substructure Geometry*

We now turn to the number and orientation of the n_{active} CBBs alluded to in Section A. Peeters *et al.* assume that each grain in bcc IF-steel forms two CBBs on the two most active {110} slip planes during deformation. They find that this condition is consistent with their TEM micrographs of CBBs. In the case of fcc metals, on the other hand, the substructure geometry has been experimentally observed to be far more complex and dependent on grain orientation and loading. Figure 2 shows four different types of substructures observed in our copper samples after 15 and 30 pct rolling reductions. As seen in this figure, and in the more extensive studies of Wert *et al.*,[39] Liu *et al.*,[40] and Liu *et al.*,[41] whether CBBs form in a grain, and if so, the number of CBBs in a grain depends upon the grain orientation and loading. Furthermore, CBB morphology may be planar or wavy, and CBBs may or may not coincide with crystallographic slip planes in copper and aluminum under a variety of loading conditions. Indeed, after a statistical study of CBB orientations after rolling, Christoffersen and Leffers[22] found

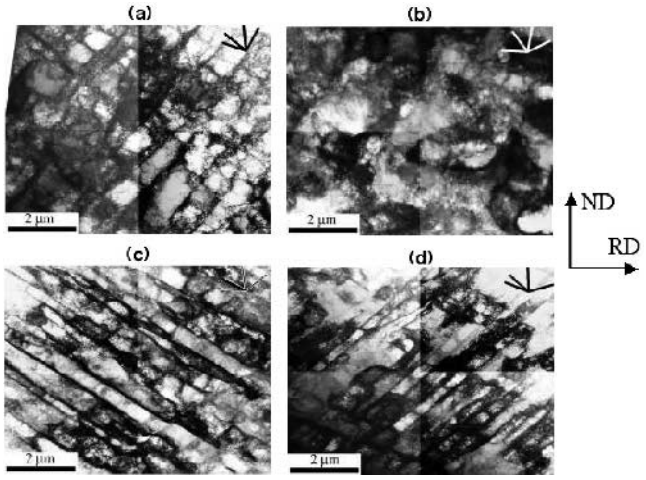

Fig. 2—Some of the dislocation substructures observed after rolling: (*a*) and (*b*) 15 pct reduction and (*c*) and (*d*) 30 pct reduction. (a) one crystallographic and one noncrystallographic set of CBBs, (b) equiaxed cell structure, (c) one set of crystallographic CBBs, and (d) two sets of noncrystallographic CBBs. The four (111) slip traces are shown in the top right corner of each micrograph.

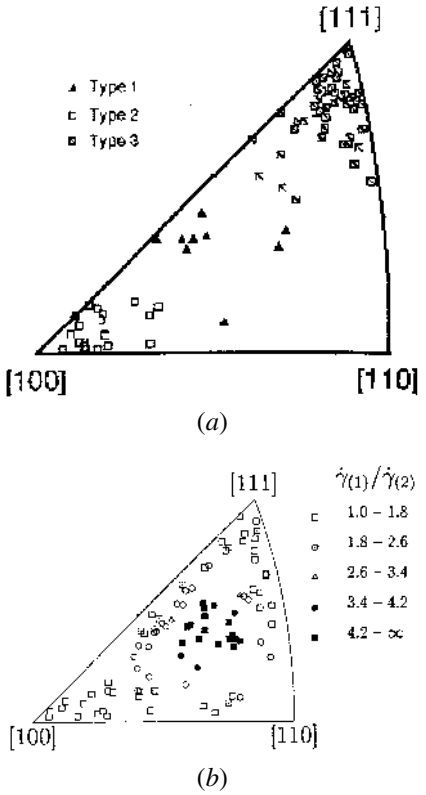

Fig. 3—(*a*) The position of the tensile axis of a grain in the inverse pole figure strongly correlates with the type of microstructure it forms (Huang,[23] Figure 1], with permission). (*b*) Ratio of the largest to the second largest slip system activity in 100 grains plotted on an inverse pole figure from a viscoplastic self-consistent simulation assuming Voce hardening. Notice that Huang's type 1 grains in (a) away from the [100]–[111] line correspond to the central region of the triangle where one slip system is substantially dominant in (b).

"Dislocation walls in copper have no preference for orientations parallel to or approximately parallel to the {111} slip planes."

While the cause of this qualitative difference between bcc and fcc behavior is unknown, it seems plausible that it arises because of the larger fraction of screw dislocations in bcc metals relative to fcc. Screw dislocations are capable of cross-slip. According to the theory of Winther *et al*.,[28] the mechanism of cross-slip will strengthen the crystallographic preference of CBBs as cross-slipping systems, may add to the slip activity in the most active slip plane. In fcc metals, however, the mixed character of a greater fraction of dislocations (incapable of cross-slip) likely lowers such crystallographic CBB preference and probably leads to the more complicated CBB patterns. However, we will see that in fcc metals also, the mechanism of cross-slip plays an important role when there is no dominant slip plane (defined in Eq [11]).

In fcc metals, Winther *et al*.[28] and Winther[29] made the important observation that "coplanar slip fraction" determines whether crystallographic CBBs form in a grain. They find that CBBs do form parallel to {111} planes if the two most active slip systems on the same plane account for most of the slip activity in the grain. Their theory, however, does not predict the orientation of CBBs when single slip plane dominance does not hold.

In crystals wherein slip plane dominance does not occur, Wert and Huang[42] have introduced the concept of an equivalent slip system pair, which is a set of two planes and directions (not necessarily coincident with any physical slip system), the slip on which can accommodate any plane strain deformation prescribed on the grain. They then show by means of extensive comparison to available experimental data that CBBs do indeed form on these equivalent slip planes, which are fed dislocations by slip activity on physical slip systems associated with each equivalent one. Wert and Huang's analysis, however, is limited to plane strain deformations of high symmetry crystal orientations (Goss, rotated cube, cube, and copper ideal texture components). Its extension to arbitrary orientations under arbitrary grain loadings is not presently available. Such an extension would be essential for implementation in the present model.

Another class of crystal plasticity models are based on the minimization of stored energy, and result in grain microstructuring (Ortiz and Repetto[43] and Ortiz *et al*.[44]). However, there appears to be no systematic comparison of their predictions of orientation dependence of microstructure against experimental observations.

In summary, while important progress in understanding CBB orientations in fcc crystals has been made, the investigation of this subject is far from closed. In this work, we pursue the following approach based on earlier results of Huang[23] and Huang and Hansen[45] for copper and aluminum, respectively. In an extensive and detailed study of microstructure evolution in OFHC copper (grain size 50 μm) tensioned up to $\varepsilon_{vM} = 0.28$, Huang[23] found a strong correlation between microstructure and grain orientation. His observation, reproduced in the inverse pole figure of Figure 3(a), is that the tensile axis of grains that form one set of crystallographic {111} CBBs (type 1) lies in the middle of the triangle, and that of grains that do not form any CBBs but only a cell substructure (type 2) lies near the [100] corner; for grains with two

sets of noncrystallographic CBBs (type 3), the tensile axes lie near the [111] corner. In a similar study on fcc aluminum (grain size 300 μm) tensioned to $\varepsilon_{vM} = 0.34$; Huang and Hansen[45] come to the same qualitative conclusion, except for observing a larger number of type 3 microstructures along the [100]-[111] line. This difference possibly arises due to the difference in grain size since they argue that the stacking fault energy difference between copper and aluminum does not affect microstructure evolution. Figure 3(b) correlates grain orientation and the slip activity in crystallographic planes during a VPSC-simulated uniaxial tensile test to $\varepsilon_{vM} = 0.28$. On an inverse pole figure, it shows the ratio of the slip activity on the most active $\left(|\dot{\gamma}_{(1)}|\right)$ and the second most active $\left(|\dot{\gamma}_{(2)}| \leq |\dot{\gamma}_{(1)}|\right)$ slip systems. Voce law hardening is assumed with parameters that fit the tension test of Figure 4 ($\tau_0 = 18$ MPa, $\tau_1 = 110$ MPa, $\theta_0 = 250$ MPa, and $\theta_1 = 12$ MPa, Eq. [1]), so as not to presuppose any set of Peeters *et al*. model parameters. As seen, the central part of the triangle corresponds to grains having a dominant slip system, *i.e*., where $|\dot{\gamma}_{(1)}/\dot{\gamma}_{(2)}| > 3.4$. Together with the aforementioned experimental observations, this implies that type 1 CBBs form in grains oriented such that $|\dot{\gamma}_{(1)}/\dot{\gamma}_{(2)}|$ is large. Grains that undergo multiple slip, on the other hand, form type 2 or type 3 microstructures; it is not possible to distinguish between these types by means of the $|\dot{\gamma}_{(1)}/\dot{\gamma}_{(2)}|$ criterion.

In the present model, we will assume the applicability of the preceding observation to arbitrary grain loadings, and assume that

$$n_{\text{active}} = \begin{cases} 1, & \text{if } |\dot{\gamma}_{(1)}/\dot{\gamma}_{(2)}| > 3.4, \\ 2, & \text{if } |\dot{\gamma}_{(1)}/\dot{\gamma}_{(2)}| \leq 3.4. \end{cases} \quad [11]$$

If there is only one active CBB, it is assumed to form on the crystallographic plane of the most active slip system. If

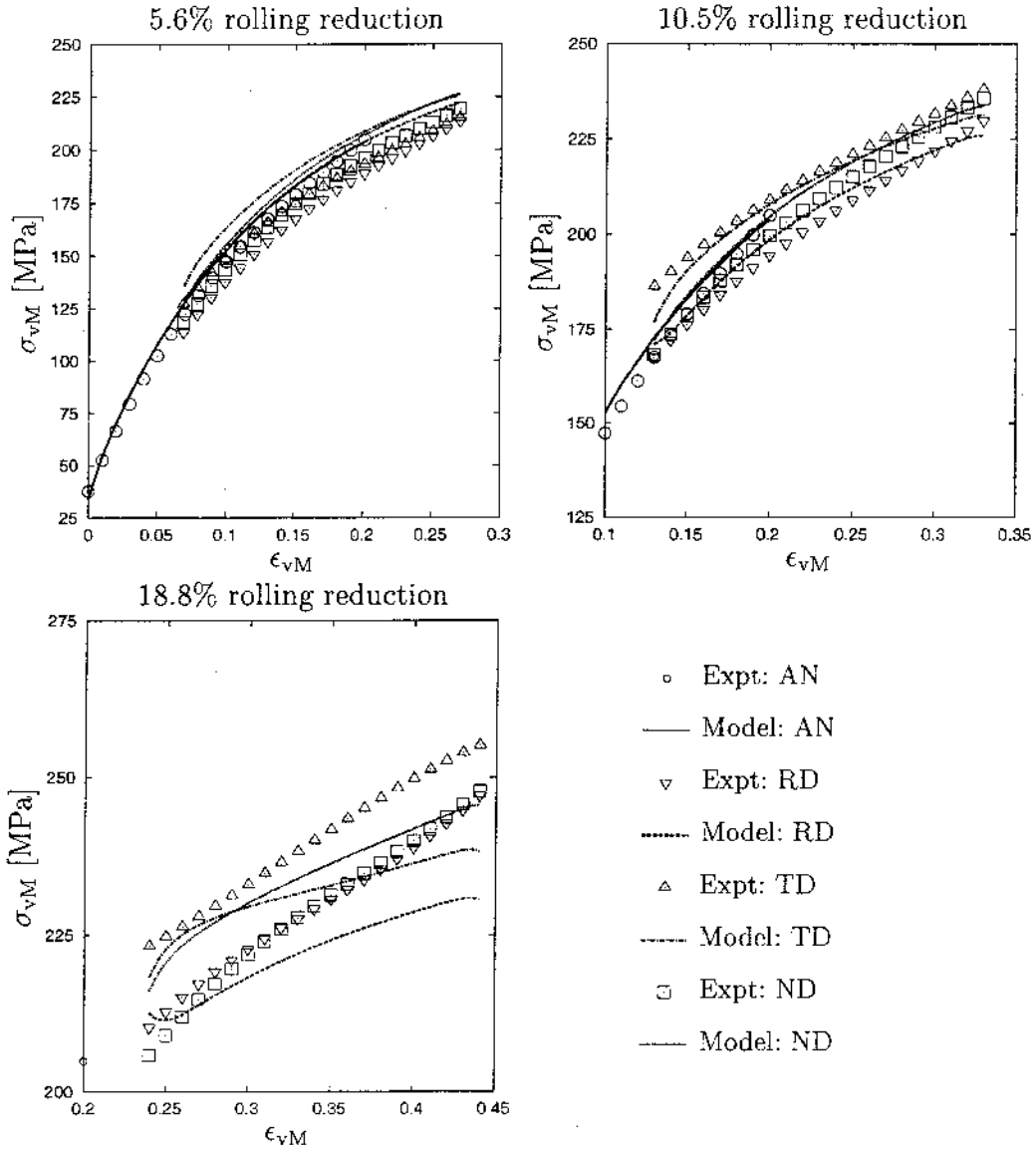

Fig. 4—Comparison of the compression experimental data along RD, TD, and ND after rolling to $r = 0$, 0.056, 0.105, and 0.188 with the model. The model parameters are *fit* to the annealed response ($r = 0$) and the TD and RD curves of $r = 0.105$. The parameters obtained are used to predict the remaining curves.

there are to be two active CBBs, they are assumed to lie on the plane of the most active slip system and its cross-slip plane. While other choices for the placement of the two CBBs are possible (*e.g.*, the crystallographic planes of the most and second most active slip systems), this choice proves essential in capturing the mechanical response upon load reversal and crossing. We will discuss this choice of CBBs further in Section IV, in connection with fitting the experimental data to the Peeters *et al.* model.

III. COMPARISON WITH EXPERIMENTS

We now describe a set of experiments that involve monotonic, reverse, and cross loading of copper against which we will compare the model of Section II. Four identical plates of OFHC copper vacuum annealed at 700 °C for 2 hours and furnace cooled over 8 hours to grain size ~100 μm were rolled to reductions of $r = 5.6$, 10.5, and 18.8 pct in one pass each. Three cylindrical specimens (length: 5.5 mm, and diameter: 7 mm) were then cut out using electrical discharge machining and from each of the four rolled plates along the rolling direction (RD), transverse direction (TD), and normal direction (ND) and were compression tested. No barreling was noticed during compression. The macroscopic strain-rate tensor during rolling is approximately $[\mathbf{D}^{(1)}] = \dot{\varepsilon}\begin{bmatrix} 1 & 0 & 0 \\ 0 & 0 & 0 \\ 0 & 0 & -1 \end{bmatrix}, (\dot{\varepsilon} \geq 0)$, expressed in the right-handed orthonormal basis defined by RD-TD-ND (≡1-2-3). Subsequent uniaxial compression with traction-free lateral surfaces along RD, TD, and ND represent a pseudo-reverse test, a pseudo-cross test, and a pseudo-monotonic test, respectively, in Barlat *et al.'s*[17] nomenclature. They are called "pseudo" since the plane strain compression in the first stage ($\mathbf{D}^{(1)}$) is replaced by uniaxial compression in the second stage.

Polycrystal calculations consisted in simulating rolling up to the same reduction as the experiments, followed by axial compression along the three principal directions. An initially random distribution of orientations was assumed and the viscoplastic self-consistent scheme for polycrystals (Lebensohn and Tomé[33]) was used.

Figure 4 compares the experimental and model-predicted stress-strain curves for compression along RD, TD, and ND after $r = 0$, 0.056, 0.105, and 0.188. Using the procedure of Appendix A, the model parameters are fit (Table II) to three experimental compression curves: compression of the annealed specimen ($r = 0$) and compression along TD and RD of the specimen rolled to $r = 0.105$. The fitting procedure is divided into two parts: keeping R_{rev} and R_2 fixed (since they do not affect monotonic or cross-test response according to Section II–A); the remaining 11 parameters are fit to the experimental stress-strain curves for annealed compression and TD compression after $r = 0.105$. Then, the fitting procedure is applied in the two-dimensional space of R_{rev} and R_2 to fit the experimental curve for compression along RD. The curve fits shown in Figure 4 are within the experimental error.

All the other curves in Figure 4 are predicted using the model supplied with these parameters, obtained from the $r = 0.105$ experimental fit. The four predicted responses for $r = 0.056$ and $r = 0.105$ are in reasonable quantitative agreement with the measured flow response. Qualitatively, while the model does capture the experimental trend, TD > ND ~ RD, it fails to capture the experimental observation that, at a given ε_{vM}, the material response is softer in compression after rolling than in compression from an annealed state. We speculate that this is because we perform numerical compression starting from a numerical rolling texture, which is known to evolve more rapidly than the experimental rolling texture.

Table II. The Model Parameters for Copper as Fit to the Three Experimental Curves Described in the Text

n_{CBB}	4
n_{active}	2
I	$2.8776 \cdot 10^{-2}$
I^{wd}	$7.2366 \cdot 10^{-1}$
I^{wp}	$1.5944 \cdot 10^{-2}$
R (m)	$1.8996 \cdot 10^{-9}$
R^{wd} (m)	$7.4544 \cdot 10^{-8}$
R^{wp} (m)	$4.7920 \cdot 10^{-10}$
R_{ncg} (m)	$3.9637 \cdot 10^{-9}$
R_{rev} (m)	$5.6487 \cdot 10^{-8}$
R_2 (m)	$9.1846 \cdot 10^{-10}$
α	$3.9772 \cdot 10^{-1}$
α'	$1.1950 \cdot 10^{-1}$
f	$1.2000 \cdot 10^{-1}$
τ^0 (MPa)	$1.2500 \cdot 10^{+1}$
b (m)	$2.5562 \cdot 10^{-10}$
G	$5.0000 \cdot 10^{+4}$

It should be pointed out that simpler models of grain substructure are unable to reproduce the transient response along RD, TD, and ND even qualitatively. A model that accounts for texture evolution but uses Eq. [1] fails even to capture the correct order of the experimental yield point trend upon load path change: TD > ND ~ RD. Also, the predictions of simpler two-parameter substructure models can be expected to follow the annealed curve (model: AN) in Figure 4; these simpler models have no mechanisms to produce the response discontinuities obtained from the present model under load reversal.

When used to predict the compression response after rolling to $r = 0.188$ ($\varepsilon_{vM} \approx 0.24$ to 0.44 during compression), the model performs poorly. While the initial yield points are reasonably well estimated, the model underestimates flow stress evolution and tends toward saturation. This is to be expected in the present stage III model when deformation enters the stage IV regime, and is consistent with the observation of Bassim and Liu[37] in copper under tension and torsion that the stage IV regime begins at $\varepsilon_{vM} \approx 0.3$.

Figure 5 shows the evolution of the dislocation densities calculated during the entire loading path in a single grain embedded in a 100-grain self-consistent computer polycrystal deformed by rolling to $r = 0.105$ ($\varepsilon_{vM} \approx 0.13$), then compressed along RD (row 1), TD (row 2), and ND (row 3). The assumed Peeters *et al.* model parameters are those used to generate Figure 4. The dominant dislocation population here is seen to be ρ whose density exceeds that of ρ^{wp} and ρ^{wd} and which therefore controls in large part the flow stress evolution in the grain. Since at the point of reversal in row 1 of Figure 5, $\rho \approx 10\rho^{wp}$ and $R \approx 10R_2$, while ρ^{wp} is seen to decrease due to the efflux of polarized dislocations from CBBs, no effect is seen in ρ since a negligible fraction of CBs suffice to annihilate the polar dislocations according to Eq. [4]. During the pseudo-reverse loading path of RD compression, the active

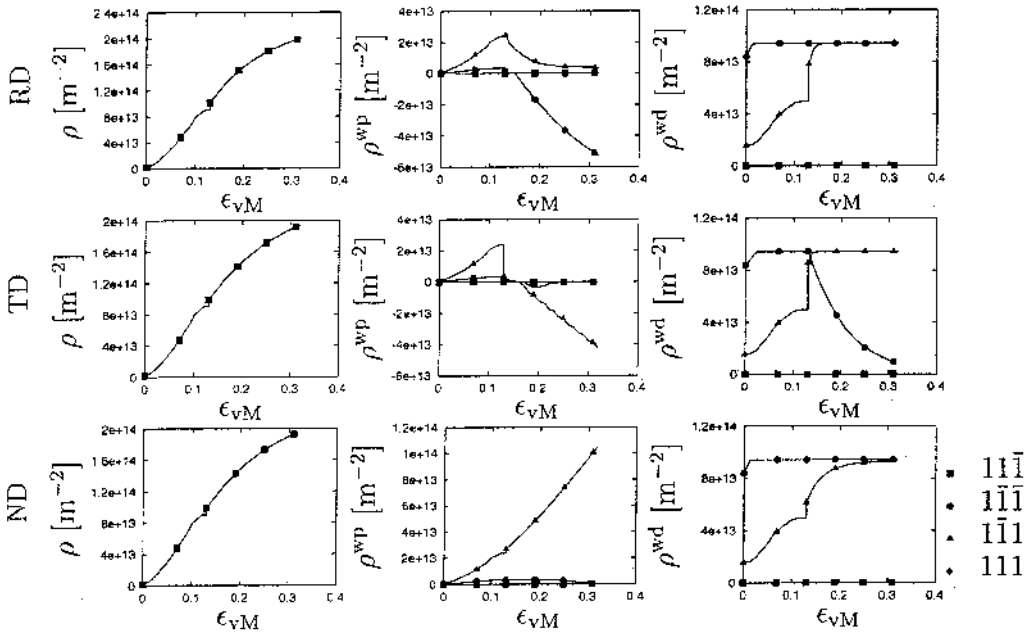

Fig. 5—Evolution of dislocation densities ρ, ρ_i^{wp}, and $\rho_i^{wd}, i = 1, \ldots, 4$ in one grain of a 100-grain model polycrystal oriented with Bunge angles (102.74, 119.56, 33.65 deg) prior to deformation in the RD-TD-ND system. The deformation path simulated here is rolling to $r = 0.105$ ($\varepsilon_{vM} \approx 0.13$), then uniaxial compression in the RD (reversal, row 1), TD (cross, row 2), and ND (monotonic, row 3) directions. Note that for compression in all three directions, the ρ approaches its saturation dislocation density of $\rho_{sat} = (I/R)^2 \approx 2.29 \cdot 10^{14}/\text{m}^2$.

slip planes during rolling, $(1\bar{1}\,\bar{1})$ and $(1\bar{1}1)$, continue to remain so. On the other hand, upon pseudo-cross loading by compression along TD (row 2), this grain switches from a state with $n_{\text{active}} = 2$ active CBBs to one with only one active CBB $(1\bar{1}1)$. Finally, note that dislocation density evolution is qualitatively sustained during pseudo-monotonic compression along ND (row 3). The calculated dislocation densities match the measurements of Hansen and Huang[46] in fcc aluminum, in order of magnitude (the measured total dislocation density is $O(10^{14})$ at $\varepsilon_{vM} = 0.2$).

IV. DISCUSSION

We will now discuss the importance of the substructural geometry assumptions of Section II–B (which represents our most significant deviation from the original bcc Peeters *et al.* model) in capturing the relatively small Bauschinger effect (~1 MPa for $r = 0.105$) and the large cross effect (~20 MPa for $r = 0.105$). Unlike in the original Peeters *et al.* model wherein every grain has $n_{\text{active}} = 2$, some (type 1) grains in the present model have only one active CBB. These grains suffer no Bauschinger effect upon load path reversal according to the model of Section II–A. To see this, observe that the most active slip system, say, s^*, is coplanar with the only active CBB, say, i^*. Since $\mathbf{u}_{s^*}^b \cdot \mathbf{u}_{i^*}^w = 0$, s^* will not contribute to dislocation flux Φ_{i^*}. The lack of Bauschinger effect in a fraction of the grains already decreases the magnitude of the macroscopic Bauschinger effect. Furthermore, even in grains with $n_{\text{active}} = 2$ placed per Section II–B, the most active slip system, say, s^*, is coplanar with either active CBB, say, i^*. The system s^* will not contribute to dislocation flux Φ_{i^*}, since $\mathbf{u}_{s^*}^b \cdot \mathbf{u}_{i^*}^w = 0$. Φ_{i^*}, and by Eq. [3] therefore $\rho_{i^*}^{wp}$ (which determines the magnitude of the Bauschinger effect), will remain small.

Contrariwise, if the active CBBs were placed on the two planes most active in slip, so that ρ^{wp} on each active CBB is fed by slip systems intersecting that CBB plane and parallel to the other, accumulated ρ^{wp} would be large, leading to a much larger Bauschinger effect than observed experimentally in copper. This argument provides support to our active CBB placement strategy.

Further support is provided by the ability of the present model to capture the large observed cross effect. In the first stage of deformation (rolling), if s^* is the most active slip system during rolling and i^* either its slip plane or cross-slip plane, $\mathbf{u}_{s^*}^b \cdot \mathbf{u}_{i^*}^w = 0$. CBB i^* does not contribute to the CRSS of slip system s^* according to Eq. [8]. In other words, s^* has an infinite mean free path ($= d_{i^*}/\mathbf{u}_{s^*}^b \cdot \mathbf{u}_{i^*}^w$, Eq. [6]) between the barriers presented by either CBB i^*.

Upon load crossing, if s^{**} becomes the dominant slip system, not coplanar with either CBB i^*, $\tau_{i^* s^{**}}^{\text{CBB}}$ will be large since $\mathbf{u}_{s^{**}}^b \cdot \mathbf{u}_{i^*}^w \neq 0$ and s^{**} has a drastically reduced mean free path between them than s^*. This will cause a large cross effect, which increases with prestrain, as observed. On the other hand, if the active CBB, i^* were as in the original Peeters *et al.* model, and the slip system s^* parallel to one CBB intersects the other, load crossing will not bring about as drastic a reduction in the mean free path, and the cross effect will be much smaller in magnitude. The present substructural geometry thus enhances the "barrier" posed to dislocation motion during a cross test along the newly activated slip system s^{**} by the CBB i^* formed during rolling, and this enhancement is essential for obtaining reasonable fits in Figure 4 (Aernoudt *et al.*[19]).

In summary, the present model, while clearly not modeling the variety of microstructural features observed experimentally in deformed fcc copper essentially captures their influence on the mechanical response using a simple CBB orientation scheme.

We next turn to another important aspect of our procedure, *viz.* the fitting of the parameters in Table II using the methodology in Appendix A. As mentioned there, the procedure produces sets of different parameters that nevertheless fit the experimental data nearly equally well. This nonuniqueness suggests the need for imposing additional constraints on the ranges of individual parameters. These constraints may come from calculations and observations at smaller length scales (*e.g.*, dislocation dynamics, or experimental studies of the rate of absorption of mobile dislocations into CBBs). The constraints may also take the form of having to fit additional stress-strain curves with the same set of parameters. Our experience in this respect is that the inherent differences in flow response arising from variations between nominally identical specimens set a limit to the accuracy of the measured stress-strain curves, which is sizable enough that one ends up obtaining poorer, still nonunique fits to them all, since this type of constraint does not restrict the range of individual parameters. For this reason, we believe that the former approach to constraining individual parameters is the superior one; indeed, the utility of the Peeters *et al.* model may lie primarily in directing research at lower length scales toward identifying parameters for use in mesoscale models such as the present one.

The present model with its detailed microstructure evolution mechanisms will be useful when fit to well-characterized experimental response of a particular material, for which it is important to capture the response to strain path change (e.g., if one is interested in predicting flow localization during sequential forming processes). However, given the dispersion in experimental data available in the literature, and the inapplicability of the parameters to materials with other alloy compositions and grain sizes, chasing a load path change effect of similar magnitude as the dispersion in the data may not be warranted. Figure 6 compares the prediction of the present model against the data of Christodoulou *et al.*[34] during uniaxial Bauschinger tests. The grain size and strain rate of the experiments to which the present model is fit (100 μm and 10^{-3}/s, respectively) differ from those of Christodoulou's experiment (20 μm and 10^{-5}/s). While displaying a Bauschinger effect comparable to the experimental one, the flow stress predictions of the model are clearly below the experimental ones. The reason is simply the flow stress scatter among different copper materials. The experimental monotonic flow stress of the copper material of the present work is about 40 MPa below that of Christodolou *et al's* at a uniaxial compressive strain of 20 pct. In addition, the model tends to saturation, while the experiment shows a type IV hardening stage. To overcome this difficulty, the present model must be extended to account for grain size, strain rate effects, and stage IV, at the expense of introducing additional parameters.

V. CONCLUSIONS

We develop a hardening model for fcc copper following the model presented by Peeters *et al.* for bcc steel. By accounting for three different dislocation populations within each grain, the present model reproduces the flow response of copper associated with monotonic loading, and strain path changes in the stage III regime. The model however breaks down in the stage IV regime. The discontinuous transition due to strain path change is assumed to be connected with either change polar dislocation density at the walls (Bauschinger effect), or the effect of interaction of old walls with new dislocation directions (cross effect). We find that texture alone cannot explain the ordering of compression curves along RD, TD, and ND of copper prestrained by rolling, and that the contribution from the directional dislocation structure also has to be accounted for.

We find that the dislocation structure in copper (and most likely in other fcc aggregates also) is more complex than bcc steel: depending on grain orientation, none, one, or two families of dislocation walls form within the grain, not necessarily on crystallographic planes. Our criteria for dealing with

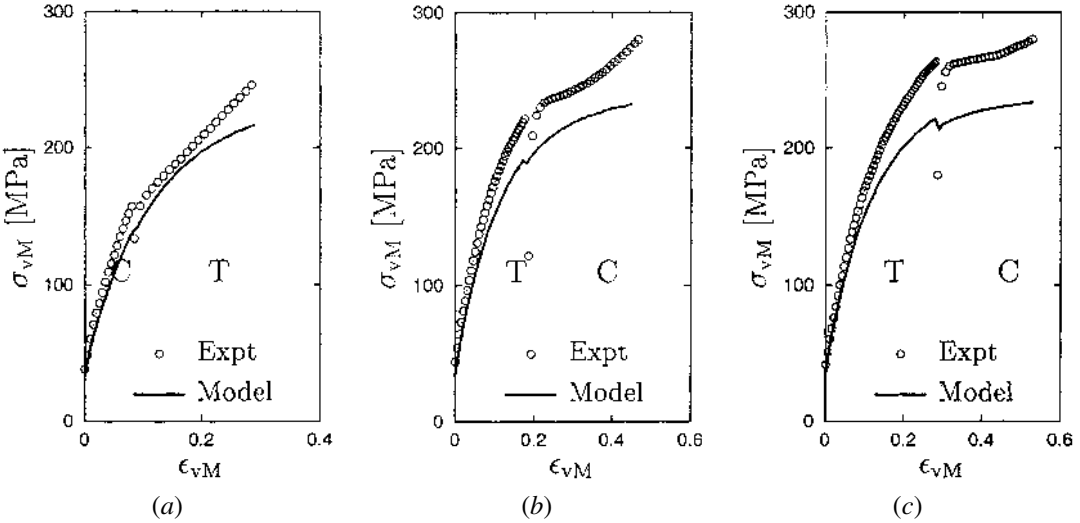

Fig. 6—Comparison of the experimental data reported by Christodoulou *et al.*[34] against the Peeters *et al.* model assuming $n_{active} = 1$ and $n_{active} = 2$. The "T" denotes tension and the "C" compression. (*a*) Compression test followed by tension. (*b*) and (*c*) Tension tests followed by compression. The parameters used in the model are reported in Table II. The gap between the experimental and model curves emphasizes the importance of the difference between the copper material and testing conditions (*e.g.*, average grain size and testing conditions) of different experiments.

such configurations is probably too simplistic, and reflects our lack of understanding of the physics behind the formation of these structures. We also find, by using our model to simulate results in the literature, that it is sensitive to composition, grain size, and strain rate.

Our study highlights the following.

1. A hardening model that can reproduce arbitrary transition effects associated with strain-path changes will be unavoidably complex, since it needs to account for the evolving dislocation substructure inside each grain with a reasonable amount of detail.
2. Approaches that attempt to determine all their parameters by fitting solely against bulk mechanical response, without an understanding of mechanisms at the dislocation scale, will suffer from nonuniqueness of best parameter sets. Such nonuniqueness may go un-noticed when parameter sets are manually fit.
3. Relating the parameters of the model with basic dislocation models and experimental characterization of the microstructure is thus essential, and the framework of the present model suggests specific questions about the interaction of families of dislocations.

ACKNOWLEDGMENTS

This research is funded by the Department of Energy, Office of Science, Office of Basic Energy Sciences. We thank Dr. M. Seefeldt for patiently clarifying aspects of the model in Reference 1.

APPENDIX

Parameter fitting

We will now describe the heuristic optimization procedure found most effective in finding material parameter sets of the hardening model used here[1] to fit a suite of experimental stress-strain curves (tests). For convenience of reference, let us assign an index i to each available test and denote it by T_i, $i = 1, 2, \ldots, n_{\text{test}}$, where n_{test} is the number of tests against which to fit. Let $\mathbf{Q} = \{Q_j, j = 1, \ldots, n_{\text{param}}\}$ denote a set of parameters. Using this set of parameters, we may numerically simulate T_i, and obtain a theoretical stress-strain curve, $\sigma_{\text{theo}}(\varepsilon)$, to compare with the corresponding experimental $\sigma_{\text{expt}}(\varepsilon)$. We then define the fitting error, or "cost," associated with the parameter set $\mathbf{Q}$ and test T_i to be

$$C(\mathbf{Q}, T_i) = \sqrt{\frac{\int (\sigma_{\text{expt}} - \sigma_{\text{theo}})^2 |d\varepsilon|}{\int |d\varepsilon|}}, \qquad [A1]$$

where both integrals run over the entire loading path. The cost associated with a fixed $\mathbf{Q}$ and T_i is thus the weighted sum of the root-mean-square errors between the experimental and theoretical stresses. Next, assigning weights w_i, $i = 1, 2, \ldots, n_{\text{test}}$ to the individual tests such that $\sum_{i=1}^{n_{\text{test}}} w_i = 1$, we define the cost associated with the parameter set $\mathbf{Q}$ over all tests in the suite T_i, $i = 1, \ldots, n_{\text{test}}$ as

$$C(\mathbf{Q}) = \sum_{i=1}^{n_{\text{test}}} w_i C(\mathbf{Q}, T_i) + \psi \max_{i=1}^{n_{\text{test}}} C(\mathbf{Q}, T_i) \qquad [A2]$$

We use $w_i = 1/n_{\text{test}}$ and $\psi = 1.25$ in our implementation. The problem of finding a good set of fitting parameters may now be stated in optimization terms as minimizing $C(\mathbf{Q})$ in the space of all valid parameter sets, which will henceforth be denoted $\mathfrak{Q}$. Since the numeric values of the parameters of the Peeters *et al.* model are several orders of magnitude apart, we operate in the space $\mathfrak{L}$ whose points are obtained by taking an element-wise logarithm of the coordinates of points in $\mathfrak{Q}$.

Three features of the cost function determine our choice of global optimization procedure. First, the cost function is extremely noisy and has a large number of local minima of similar depth in $\mathfrak{Q}$. Second, cost function evaluation is very expensive, as it involves simulating the entire deformation paths of several tests while holding $\mathbf{Q}$ fixed. Finally, derivatives of the cost function in $\mathfrak{Q}$ can only be obtained by numerical means and are prohibitively expensive as their evaluation will involve at least $n_{\text{param}} + 1$ function evaluations. The noisiness of the cost function also makes numerical derivatives so calculated completely useless in choosing a search direction.

The constraints listed previously in the present optimization problem were also encountered by Brachetti et al.[47] while attempting to fit a model to data for eclipsing binary stars. After extensive study reported there, they find Price's algorithm[48] best suited for their purpose. They go further and modify Price's algorithm to accelerate its convergence. We do not implement this accelerated methodology, since the quadratic approximation of the cost used in it is ill suited to our case where the basins of convergence around minima are small. Therefore, our approach to global minimization in the present problem consists of finding "promising regions" of $\mathfrak{Q}$ using Price's algorithm and then to search for the minima within these regions using the simplex algorithm (Nelder and Mead,[49] Spendley et al.,[50] and Fletcher[51]). Our sequential approach is illustrated schematically in Figure A1.

As prescribed by Price, we sample a compact set $\mathfrak{D} \subset \mathfrak{L}$ shaped as an n_{param}-dimensional hypercube centered at the Peeters *et al.* parameters for IF steel with a side dimension of log 20, with random points $\mathbf{Q}_k^{(0)}$, $k = 1, \ldots, 25\, n_{\text{param}}$, and evaluate the cost $C(\mathbf{Q}_k^{(0)})$ at each of them. We then follow Price's iterative algorithm, as described in Reference 47 to displace the original sample points $\mathbf{Q}_k^{(0)}$ to new coordinates $\mathbf{Q}_k^P$ such that $C(\mathbf{Q}_k^P) \le C(\mathbf{Q}_k^{(0)})$. Briefly, the lth iteration of Price's algorithm consists of reflecting the sample point with the highest cost, $\mathbf{Q}_{k_1}^{(l-1)}: C(\mathbf{Q}_{k_1}^{(l-1)}) = \max_k C(\mathbf{Q}_k^{(l-1)})$ about the centroid of a random collection of $n_{\text{param}} + 1$ other sample points and repeating with a different set of random points until $C(\mathbf{Q}_{k_1}^{(l)}) < C(\mathbf{Q}_{k_1}^{(l-1)})$. Each iterative step of this algorithm thus reduces the maximum cost of the sample at that iteration, $\max_k C(\mathbf{Q}_k^{(l-1)})$ and potentially also lowers $\min_k C(\mathbf{Q}_k^{(l-1)})$ if $C(\mathbf{Q}_{k_1}^{(l)}) < \min_k C(\mathbf{Q}_k^{(l-1)})$.

The original Price's algorithm terminates at iteration l^* if the range of costs $\max_k C(\mathbf{Q}_k^{(l^*)}) - \min_k C(\mathbf{Q}_k^{(l^*)})$ goes below a predetermined tolerance. In our application, however, we find this condition is not attained within reasonable computation time (10 days on an i686 PC). It appears that the algorithm displaces the original sample points to the vicinity of several approximately equal minima, as shown in Figure A1(b), and reflecting a displaced sample point about other points not in its cluster places it in a region of high cost with large certainty. It may be possible to rectify this situation by substantially

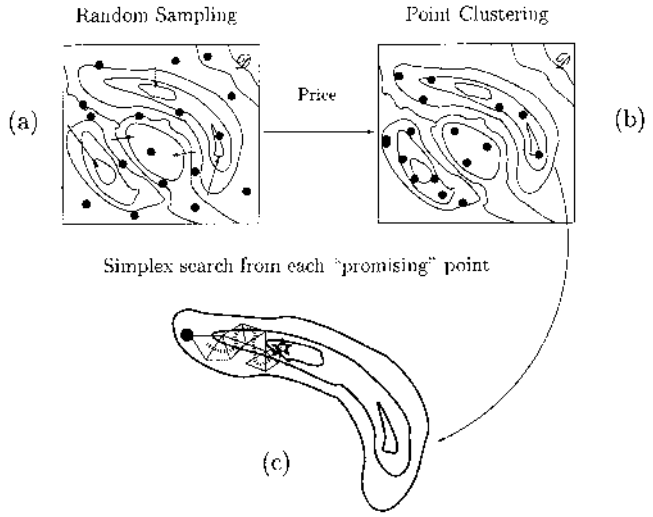

Fig. A1—Schematic depicting the global minimization procedure used. (*a*) A uniform sampling $(\mathbf{Q}_k^{(0)})$ of $\mathfrak{D} \subset \mathfrak{L}$ is shown. Contours represent lines of constant cost.-function value, and arrows represent the direction of decreasing cost. (*b*) The new positions of the initial sampling points $(\mathbf{Q}_k^P)$ after the action of Price's algorithm. The new points are now concentrated in "promising" regions, while not necessarily achieving the global minimum. (*c*) Progress of the simplex algorithm starting at one of the promising points in (b) (circle) to the nearby local minimum (star). This procedure is repeated from each of the promising points in (b), and the local minimum with the least cost is considered the global minimum.

increasing the number of initial sample points. However, for keeping computation times reasonable, we terminate Price's algorithm when either Price's original termination condition is met or when it fails to advance after a cut-off number of point flipping trials (200). If termination is reached after l^* iterations, we call $\mathbf{Q}_k^P \equiv \mathbf{Q}_k^{(l^*)}$ the Price-generated promising points.

We proceed onward with the simplex algorithm starting from each of the $\mathbf{Q}_k^P$. In brief, the simplex algorithm constructs an $(n_{\text{param}} + 1)$-sided simplex, or a regular solid (equilateral triangle in two dimensions, regular tetrahedron in three dimensions, etc.) in $\mathfrak{L}$, with $\mathbf{Q}_k^P$ as one of the vertices. Each of the other n_{param} vertices is obtained by perturbing precisely one of the coordinates of $\mathbf{Q}_k^P$ by $\pm \log c$, where the sign is decided either way randomly with probability half. By trial and error, we find $c = 1.2$ satisfactory. The simplex algorithm also involves point flipping of the vertex with maximum cost across the centroid of the other vertices of the simplex (Figure A1(c)). After a simplex vertex has remained in it in excess of a cut-off number of flips (15), we halve each edge of the simplex about the vertex with minimum cost (Fletcher[51]) and continue vertex flipping with this smaller simplex. After three successive halvings, the simplex algorithm terminates, and the vertex with least cost is taken to be a local minimum near $\mathbf{Q}_k^P$. The preceding simplex algorithm is repeated for $k = 1, \ldots, 25\, n_{\text{param}}$ to generate several local minima. The local minimum with the least cost is then taken to be the global minimum. The cost at the so-defined global minimum is usually only insignificantly lower than the cost at a few other local minima. The global minimum is thus practically nonunique; disparate parameter sets generate similar stress-strain responses with similar costs.

As stated at the outset, the cost-minimizing algorithm described here is a heuristic method. The minimum found has no theoretical guarantee of being global optimal. Also, we sample a very large set $\mathfrak{D}$ with relatively few points, so that we can expect at best to arrive at a good approximation of the global minimum cost. Nevertheless, the preceding method of determining parameters represents a significant improvement over manual curve fitting.

REFERENCES

1. B. Peeters, M. Seefeldt, C. Teodosiu, S.R. Kalidindi, P.V. Houtte, and E. Aernoudt: *Acta Mater.*, 2001, vol. 49, pp. 1607-19.
2. B. Peeters, B. Bacroix, C. Teodosiu, P.V. Houtte, and E. Aernoudt: *Acta Mater.*, 2001, vol. 49, pp. 1621-32.
3. S. Balasubramanian and L. Anand: *Acta Mater.*, 2002, vol. 50, pp. 133-48.
4. C. Tomé, G.R. Canova, U.F. Kocks, N. Christodoulou, and J.J. Jonas: *Acta Metall.*, 1984, vol. 32 (10), pp. 1637-53.
5. C.N. Tomé, P.J. Maudlin, R.A. Lebensohn, and G.C. Kaschner: *Acta Mater.*, 2001, vol. 49, pp. 3085-96.
6. S. Kok, A.J. Beaudoin, and D.A. Tortorelli: *Int. J. Plasticity*, 2002, vol. 18, pp. 715-41.
7. U.F. Kocks, P. Franciosi, and M. Kawai: *Textures Microstr.*, 1991, vols. 14–18, pp. 1103-14.
8. U. Kocks and H. Mecking: *Progr. Mater. Sci.*, 2003, vol. 48, pp. 171-273.
9. C. Teodosiu and Z. Hu: *Proc. Numiform '95 on Simulation of Materials Processing: Theory, Methods and Applications*, S. Shen and P.R. Dawson, eds., Balkema, Rotterdam, 1995, pp. 173-82.
10. P. Hähner: *Scripta Mater.*, 2002, vol. 47, pp. 705-11.
11. W. Pantleon: *Acta Mater.*, 1998, vol. 46 (2), pp. 451-56.
12. Y. Estrin, L.S. Tóth, A. Molinari, and Y. Bréchet: *Acta Mater.*, 1998, vol. 46, pp. 5509-22.
13. L.S. Tóth, A. Molinari, and Y. Estrin: *J. Eng. Mater. Technol.*, 2002, vol. 124, pp. 71-77.
14. S.C. Baik, Y. Estrin, H.S. Kim, and R.J. Hellmig: *Mater. Sci. Eng.*, 2003, vol. A351, pp. 86-97.
15. J.J. Gracio, E.F. Rauch, F. Barlat, A.B. Lopes, and J.F. Duarte: *Key Eng. Mater.*, 2002, vols. 230–232, pp. 521-24.
16. E.F. Rauch, J.J. Gracio, F. Barlat, A.B. Lopes, and J.F. Duarte: *Scripta Mater.*, 2002, vol. 46 (12), pp. 881-86.
17. F. Barlat, J.F. Duarte, J.J. Gracio, A.B. Lopes, and E.F. Rauch: *Int. J. Plasticity*, 2003, vol. 19, pp. 1215-44.
18. A.B. Lopes, F. Barlat, J.J. Gracio, J.F.F. Duarte, and E.F. Rauch: *Int. J. Plasticity*, 2003, vol. 19, pp. 1-22.
19. E. Aernoudt, P. van Houtte, and T. Leffers: *Deformation and Textures of Metals at Large Strain*, VCH, New York, NY, 1992, vol. 6, pp. 89-136.
20. A.S. Malin and M. Hatherly: *Met. Sci.*, 1979, vol. 13, pp. 463-72.
21. J.G. Sevillano and F. Torrealdea: *Deformation of Polycrystals*, Riso National Laboratory, Roskilde, 1981, p. 185.
22. H. Christoffersen and T. Leffers: *Scripta Mater.*, 1997, vol. 37 (12), pp. 2041-46.
23. X. Huang: *Scripta Mater.*, 1998, vol. 38 (11), pp. 1697-703.
24. B. Bay, N. Hansen, and D. Kuhlmann-Wilsdorf: *Mater. Sci. Eng. A*, 1989, vol. 113, pp. 385-97.
25. D.A. Hughes and W.D. Nix: *Metall. Trans. A*, 1988, vol. 19A, pp. 3013-24.
26. D.A. Hughes and N. Hansen: *Metall. Trans.*, 1993, vol. 24 A, pp. 2021-37.
27. D.A. Hughes and N. Hansen: *Acta Mater.*, 2000, vol. 48, pp. 2985-3004.
28. G. Winther, D.J. Jensen, and N. Hansen: *Acta Mater.*, 1997, vol. 45 (12), pp. 5059-68.
29. G. Winther: *Acta Mater.*, 2003, vol. 51, pp. 417-29.
30. U.F. Kocks, A.S. Argon, and M.F. Ashby: *Progress in Materials Science, Thermodynamics and Kinetics of Slip*, Pergamon Press, New York, NY, 1975.
31. L.P. Kubin and J. Lépinoux: in *Strength of Metals and Alloys (ICSMA 8)*, P.O. Kettunen, T.K. Lepistö, and M.E. Lehtonen, eds., Pergamon Press, New York, NY, 1988, vol. 1, pp. 35-59.
32. L.P. Kubin: *Dislocation Patterning*, VCH, New York, NY, 1992, 138-87.
33. R.E. Lebensohn and C.N. Tomé: *Acta Metall. Mater.*, 1993, vol. 41 (9), pp. 2611-24.
34. N. Christodoulou, O.T. Woo, and S.R. MacEwen: *Acta Metall.*, 1986, vol. 34 (8), pp. 1553-62.

35. A.S. Argon and P. Haasen: *Acta Metall. Mater*., 1993, vol. 41 (11), pp. 3289-306.
36. A. Godfrey and D.A. Hughes: *Acta Metall. Mater*., 2000, vol. 48 (8), pp. 1897-905.
37. M.N. Bassim and C.D. Liu: *Mater. Sci. Eng. A*, 1993, vol. A164, pp. 170-74.
38. U.F. Kocks, C.N. Tomé, and H.-R. Wenk: *Texture and Anisotropy*, Cambridge University Press, Cambridge, United Kingdom, 1998.
39. J.A. Wert, Q. Liu, and N. Hansen: *Acta Metall. Mater*., 1995, vol. 43 (11), pp. 4153-63.
40. Q. Liu, D.J. Jensen, and N. Hansen: *Acta Mater*., 1998, vol. 46 (16), pp. 5819-38.
41. Q. Liu, X. Huang, D.J. Lloyd, and N. Hansen: *Acta Mater*., 2002, vol. 50, pp. 3789-802.
42. J.A. Wert and X. Huang: *Phil. Mag*., 2003, vol. 83 (8), pp. 969-83.
43. M. Ortiz and E.A. Repetto: *J. Mech. Phys Solids*, 1999, vol. 47, pp. 397-462.
44. M. Ortiz, E.A. Repetto, and L. Stainier: *J. Mech. Phys. Solids*, 2000, vol. 48, pp. 2077-2114.
45. X. Huang and N. Hansen: *Scripta Mater*., 1997, vol. 37 (1), pp. 1-7.
46. N. Hansen and X. Huang: *Acta Mater*., 1998, vol. 46 (5), pp. 1827-36.
47. P. Brachetti, M.D. Ciccoli, G. DiPillo, and S. Lucidi: *J. Global Optimiz*., 1997, vol. 10 (2), pp. 165-84.
48. W.L. Price: in *Towards Global Optimization*, L.C.W. Dixon and G.P. Szegö, eds., North-Holland, Amsterdam, 1978, vol. 2.
49. J.A. Nelder and R. Mead: *Comput. J*., 1965, pp. 303-13.
50. W. Spendley, G.R. Hext, and F.R. Himsworth: *Technometrics*, 1962, vol. 4, pp. 441-61.
51. R.A. Fletcher: *Practical Methods of Optimization*, vol 1, *Unconstrained Optimization*, John Wiley & Sons, New York, NY, 1980.